View metadata, citation and similar papers at core.ac.uk

brought to you by CORE

provided by Elsevier - Publisher Connector

NeuroImage 142 (2016) 522–532

Contents lists available at ScienceDirect

NeuroImage

journal homepage: www.elsevier.com/locate/ynimg

The link between diffusion MRI and tumor heterogeneity: Mapping cell eccentricity and density by diffusional variance decomposition (DIVIDE)

Filip Szczepankiewicz [a,*], Danielle van Westen [b,c], Elisabet Englund [d], Carl-Fredrik Westin [e], Freddy Ståhlberg [a,b], Jimmy Lätt [c], Pia C. Sundgren [b], Markus Nilsson [b,f]

[a] Lund University, Department of Clinical Sciences Lund, Medical Radiation Physics, Lund, Sweden
[b] Lund University, Skåne University Hospital, Department of Clinical Sciences Lund, Diagnostic Radiology, Lund, Sweden
[c] Skåne University Hospital, Department of Imaging and Function, Lund, Sweden
[d] Lund University, Skåne University Hospital, Department of Clinical Sciences Lund, Division of Oncology and Pathology, Lund, Sweden
[e] Harvard Medical School, Brigham and Women's Hospital, Department of Radiology, Boston, MA, USA
[f] Lund University, Lund University Bioimaging Center, Lund, Sweden

ARTICLE INFO

Article history:
Received 29 April 2016
Accepted 16 July 2016
Available online 20 July 2016

Keywords:
Tumor heterogeneity
Microscopic anisotropy
Diffusional variance
Diffusional kurtosis
Diffusion tensor distribution
Quantitative microscopy

ABSTRACT

The structural heterogeneity of tumor tissue can be probed by diffusion MRI (dMRI) in terms of the variance of apparent diffusivities within a voxel. However, the link between the diffusional variance and the tissue heterogeneity is not well-established. To investigate this link we test the hypothesis that diffusional variance, caused by microscopic anisotropy and isotropic heterogeneity, is associated with variable cell eccentricity and cell density in brain tumors. We performed dMRI using a novel encoding scheme for diffusional variance decomposition (DIVIDE) in 7 meningiomas and 8 gliomas prior to surgery. The diffusional variance was quantified from dMRI in terms of the total mean kurtosis (MK_T), and DIVIDE was used to decompose MK_T into components caused by microscopic anisotropy (MK_A) and isotropic heterogeneity (MK_I). Diffusion anisotropy was evaluated in terms of the fractional anisotropy (FA) and microscopic fractional anisotropy (μFA). Quantitative microscopy was performed on the excised tumor tissue, where structural anisotropy and cell density were quantified by structure tensor analysis and cell nuclei segmentation, respectively. In order to validate the DIVIDE parameters they were correlated to the corresponding parameters derived from microscopy. We found an excellent agreement between the DIVIDE parameters and corresponding microscopy parameters; MK_A correlated with cell eccentricity ($r = 0.95$, $p < 10^{-7}$) and MK_I with the cell density variance ($r = 0.83$, $p < 10^{-3}$). The diffusion anisotropy correlated with structure tensor anisotropy on the voxel-scale (FA, $r = 0.80$, $p < 10^{-3}$) and microscopic scale (μFA, $r = 0.93$, $p < 10^{-6}$). A multiple regression analysis showed that the conventional MK_T parameter reflects both variable cell eccentricity and cell density, and therefore lacks specificity in terms of microstructure characteristics. However, specificity was obtained by decomposing the two contributions; MK_A was associated only to cell eccentricity, and MK_I only to cell density variance. The variance in meningiomas was caused primarily by microscopic anisotropy (mean ± s.d.) $MK_A = 1.11 \pm 0.33$ vs $MK_I = 0.44 \pm 0.20$ ($p < 10^{-3}$), whereas in the gliomas, it was mostly caused by isotropic heterogeneity $MK_I = 0.57 \pm 0.30$ vs $MK_A = 0.26 \pm 0.11$ ($p < 0.05$). In conclusion, DIVIDE allows non-invasive mapping of parameters that reflect variable cell eccentricity and density. These results constitute convincing evidence that a link exists between specific aspects of tissue heterogeneity and parameters from dMRI. Decomposing effects of microscopic anisotropy and isotropic heterogeneity facilitates an improved interpretation of tumor heterogeneity as well as diffusion anisotropy on both the microscopic and macroscopic scale.

© 2016 The Authors. Published by Elsevier Inc. This is an open access article under the CC BY-NC-ND license (http://creativecommons.org/licenses/by-nc-nd/4.0/).

Introduction

Tumors exhibit structural heterogeneity on the macroscopic and microscopic scale. The cell morphology and cytoarchitecture is determined by the tumor origin, and depends on factors such as local oxygen gradients, nutritional and growth factors, metabolites, genetically divergent clones, and interactions with other tissues (Marusyk and Polyak, 2010). Although histopathological examination of the excised tissue is

* Corresponding author at: Lund University, Dept. of Clinical Sciences, Medical Radiation Physics, Lund, Barnvägen 2A, 22185, Lund, Sweden.
E-mail addresses: filip.szczepankiewicz@med.lu.se, filip.szczepankiewicz@gmail.com (F. Szczepankiewicz).

http://dx.doi.org/10.1016/j.neuroimage.2016.07.038
1053-8119/© 2016 The Authors. Published by Elsevier Inc. This is an open access article under the CC BY-NC-ND license (http://creativecommons.org/licenses/by-nc-nd/4.0/).

the gold standard for the clinical diagnosis, valuable information on the tissue microstructure and its heterogeneity can be probed non-invasively by diffusion MRI (dMRI) (Le Bihan, 2013; Padhani et al., 2009). For example, gross tumor heterogeneity can be estimated from the distribution of apparent diffusion coefficients (ADC) across the whole tumor (Ryu et al., 2014; Wang et al., 2012), where the ADC in each imaging voxel reflects characteristics such as the average tumor cellularity (Chenevert et al., 2000; Padhani et al., 2009), extent of infiltration (Sternberg et al., 2014), and treatment response (Moffat et al., 2005). However, the ADC is an average metric that does not capture heterogeneity within individual voxels. Hence, the ADC may be equal in homogeneous tissue and in tissue with densely packed cells interspersed with loose necrotic regions. In previous studies, heterogeneity has been probed by assigning a distribution of apparent diffusivities to each voxel and relating the variance of the distribution to the tissue heterogeneity. For example, diffusional kurtosis imaging (DKI) (Jensen et al., 2005) probes heterogeneity in terms of a normalized variance metric called the diffusional kurtosis. The kurtosis has been used to differentiate low and high grade gliomas, where increased heterogeneity was related to higher malignancy (Raab et al., 2010; Tietze et al., 2015; Van Cauter et al., 2012). However, the interpretation of diffusional variance parameters, such as the mean kurtosis, is challenging, and its link to relevant features of the underlying microstructure remain unclear (Jespersen et al., 2010; Le Bihan, 2013; Maier et al., 2010; Tietze et al., 2015; Wu and Cheung, 2010).

We argue that the link between dMRI parameters and tissue heterogeneity can be better understood by considering two separate components of the diffusional variance. The anisotropic variance component reflects the diffusion anisotropy on the microscopic scale, e.g., due to eccentric cells and cell structures (microscopic anisotropy), whereas the isotropic variance component reflects heterogeneous isotropic diffusivity, e.g., due to variable cell density or tissue mixtures (isotropic heterogeneity) (Szczepankiewicz et al., 2015; Westin et al., 2016). Although these two sources of diffusional variance originate from markedly different microstructural features, they cannot be separated by techniques based on conventional single diffusion encoding (SDE), i.e., encoding along a single direction for each signal acquisition, because such encoding conflates the effects of microscopic anisotropy and isotropic heterogeneity (Mitra, 1995). Instead, these features can be separated by performing experiments with varying 'shapes' of the diffusion encoding tensor (Westin et al., 2016). In this work, we exploit the contrast between conventional and isotropic diffusion encoding to separate the effects of microscopic anisotropy and isotropic heterogeneity, as recently proposed by Lasič et al. (2014). The conventional and isotropic encoding will be denoted 'linear' and 'spherical' tensor encoding (LTE and STE) to comply with the nomenclature proposed by Westin et al. (2016), and we will refer to methods aimed at separating the two sources of variance as 'diffusional variance decomposition' (DIVIDE).

Microscopic diffusion anisotropy has been previously estimated by employing double diffusion encoding (DDE) (Callaghan and Komlosh, 2002; Jensen et al., 2014; Jespersen et al., 2013; Lawrenz et al., 2010; Ozarslan and Basser, 2008; Shemesh et al., 2010), however, the isotropic component has so far only been reported in a limited number of studies (Lasič et al., 2014; Szczepankiewicz et al., 2015; Westin et al., 2016). The link between dMRI and the underlying tissue microstructure has been studied by comparing several dMRI parameters to corresponding features observed by qualitative and quantitative microscopy. Human studies are scarce due to the invasive nature of resection and biopsies but initial studies have shown a relation between diffusion anisotropy and tissue microstructure in brain (Ronen et al., 2014), tumor (Szczepankiewicz et al., 2015) and prostate tissue (Bourne et al., 2012). In animals, the investigated features range across structure eccentricity and orientation (Budde and Frank, 2012; Khan et al., 2015; Schilling et al., 2016), neurodegeneration (Jelescu et al., 2016; Jespersen et al., 2010; Kamagata et al., 2016), and axonal diameter (Barazany et al., 2009). However, the link between microscopic tissue heterogeneity and diffusional variance has not yet been studied.

The purpose of this study was therefore to investigate the link between diffusional variance and tissue heterogeneity in tumors. We use DIVIDE to assess the presence of microscopic anisotropy and isotropic heterogeneity, and we correlate these measures to cell eccentricity and density derived from quantitative microscopy. The study was performed in meningiomas and gliomas because these tumors exhibit a wide range of microstructural features that contribute to relevant aspects of the diffusional variance (Szczepankiewicz et al., 2015). We observed a strong correlation between microscopic anisotropy and cell eccentricity, as well as between isotropic heterogeneity and cell density variance.

Theory

The microscopic anisotropy and isotropic heterogeneity of tissue can be quantified by considering that each imaging voxel contains an ensemble of microenvironments. We model the diffusion within each microenvironment by a microscopic diffusion tensor, and the ensemble is therefore modelled by a distribution of microscopic diffusion tensors ($\mathbf{D}$) (Jespersen et al., 2013; Lasič et al., 2014; Topgaard, 2016; Westin et al., 2016). This representation assumes Gaussian diffusion in each microenvironment, which is accurate for moderate signal attenuation, i.e., for encoding strengths where at least 10% of the initial signal remains, for diffusion times that are long relative to the size of the restrictions (Topgaard and Söderman, 2003). Averaging across the distribution of microscopic tensors in a voxel yields a single voxel-scale tensor, $\langle\mathbf{D}\rangle$, equivalent to the tensor derived from diffusion tensor imaging (DTI) (Basser et al., 1994), where the averaging operation is denoted by $\langle\cdot\rangle$. Although the voxel scale diffusion tensor is useful in a plethora of applications (Alexander et al., 2007), it does not retain information on the heterogeneity of the underlying distribution of diffusion tensors. To retain such information, the distribution of diffusion tensors can be parameterized in terms of its mean diffusivity and two components of diffusional variance. The mean diffusivity (MD) is defined from the distribution of isotropic diffusivities ($D_\mathrm{I} = \mathrm{E}_\lambda[\mathbf{D}]$) averaged across all microenvironments in a voxel, according to

$$\mathrm{MD} = \langle \mathrm{D}_\mathrm{I} \rangle = \langle \mathrm{E}_\lambda[\mathbf{D}] \rangle = \mathrm{E}_\lambda[\langle \mathbf{D} \rangle], \tag{1}$$

where the average over tensor eigenvalues is denoted $\mathrm{E}_\lambda[\cdot]$. We note that MD in Eq. 1 is not affected by the order in which the averaging is applied, i.e., across eigenvalues or microenvironment tensors first. Unlike DKI, where specific sources of diffusional variance are not considered (Jensen et al., 2005), diffusional variance decomposition is used to separate the diffusional variance into two components: the anisotropic and isotropic variance (V_A and V_I), where the total variance (V_T) is simply the sum of its components ($V_\mathrm{T} = V_\mathrm{I} + V_\mathrm{A}$) (Lasič et al., 2014; Szczepankiewicz et al., 2015). The isotropic heterogeneity is related to the isotropic variance, according to

$$V_\mathrm{I} = \mathrm{V}[D_\mathrm{I}] = \mathrm{V}[\mathrm{E}_\lambda[\mathbf{D}]], \tag{2}$$

where $\mathrm{V}[\cdot]$ is the variance operator. We note that V_I is zero for tissues where all microenvironments exhibit identical isotropic diffusivity. The value of V_I for the voxel-scale tensor, $\langle\mathbf{D}\rangle$, is zero by definition since the isotropic diffusion of $\langle\mathbf{D}\rangle$ is defined by a scalar MD, and will therefore not be considered beyond this point. The anisotropic variance is related to the microscopic anisotropy, according to

$$V_\mathrm{A} = \frac{2}{5}\langle \mathrm{V}_\lambda, [\mathbf{D}] \rangle, \tag{3}$$

where the factor 2/5 relates the eigenvalue population variance, denoted by the operator $\mathrm{V}_\lambda[\cdot]$, to the variance of the distribution of diffusivities in the powder sample (Topgaard, 2016). We note that V_A is zero

for tissue that comprises only isotropic microenvironments, and that the voxel-scale counterpart is closely related to the voxel-scale anisotropy, as described below.

An inherent limitation of conventional dMRI, performed with so-called single diffusion encoding, here referred to as linear tensor encoding, is that it cannot be used to distinguish the two sources of variance (Mitra, 1995). To disentangle the two sources of variance, DIVIDE employs diffusion encoding tensors (**B**) with multiple shapes, namely linear and spherical encoding tensors, i.e., LTE and STE. Linear tensor encoding yields a 'stick' shape (**B** has one non-zero eigenvalue), for which the signal is sensitive to the total variance since both isotropic heterogeneity and microscopic anisotropy contribute to the variance of the underlying distribution of diffusivities. Spherical tensor encoding yields a 'sphere' shape (**B** has three equal eigenvalues), which removes the effects of microscopic anisotropy making the signal sensitive only to the variance due to isotropic heterogeneity (Eriksson et al., 2013; Lasič et al., 2014; Szczepankiewicz et al., 2015). The benefit of introducing multiple tensor shapes is visualized in Fig. 1, where three radically different microstructures are indistinguishable by LTE alone, but can be separated when both STE and LTE are employed. Notably, DIVIDE is compatible with arbitrary tensor shapes, enabled by techniques such as free gradient waveforms modulation or double diffusion encoding, as long as more than one shape is employed (Eriksson et al., 2015; Topgaard, 2016; Westin et al., 2016). In summary, LTE probes V_T, whereas STE probes V_I, as exemplified in Fig. 1, and V_A is recovered by simply subtracting the isotropic variance from the total variance ($V_A = V_T - V_I$) (Lasič et al., 2014; Szczepankiewicz et al., 2015).

We emphasize that the term 'diffusional variance' refers to the same phenomenon as intended by 'diffusional kurtosis' (from DKI), and in keeping with the formalism presented by Jensen et al. (2005), we normalize and scale the diffusional variance, according to

$$\mathrm{MK_x} = 3 \cdot \frac{V_x}{\mathrm{MD}^2}, \tag{4}$$

where the subscript 'x' denotes the specific component that it reflects. For example, $\mathrm{MK_I}$ denotes the normalized variance due to isotropic heterogeneity.

The macroscopic and microscopic fractional anisotropy, i.e., FA (Basser et al., 1994; Basser and Pierpaoli, 1996) and μFA (Lasič et al., 2014; Westin et al., 2016), can also be written in terms of the eigenvalue expectance and variance, according to

$$\mathrm{FA}^2 = \frac{3}{2} \cdot \frac{\mathrm{V}_\lambda[\langle \mathbf{D} \rangle]}{\mathrm{E}_\lambda[\langle \mathbf{D} \rangle]^2 + \mathrm{V}_\lambda[\langle \mathbf{D} \rangle]}, \tag{5}$$

$$\mu\mathrm{FA}^2 = \frac{3}{2} \cdot \frac{\langle \mathrm{V}_\lambda[\mathbf{D}] \rangle}{\left\langle \mathrm{E}_\lambda[\mathbf{D}]^2 \right\rangle + \langle \mathrm{V}_\lambda[\mathbf{D}] \rangle}. \tag{6}$$

The distinction between macroscopic and microscopic anisotropy is defined by the stage at which the averaging operation is applied. Averaging over tensors first, as denoted by $\langle \mathbf{D} \rangle$, probes the macroscopic anisotropy, whereas averaging over variance and expectancy first, as denoted by $\langle \mathrm{V}_\lambda[\mathbf{D}] \rangle$ and $\langle \mathrm{E}_\lambda[\mathbf{D}]^2 \rangle$, probes the microscopic anisotropy. Note that the order of averaging across eigenvalues is no longer arbitrary since the expected value is squared, i.e., $\mathrm{E}_\lambda[\langle \mathbf{D} \rangle]^2 \neq \langle \mathrm{E}_\lambda[\mathbf{D}]^2 \rangle$ unless $V_I = 0$, since (Westin et al., 2016)

$$V_I = \left\langle \mathrm{E}_\lambda[\mathbf{D}]^2 \right\rangle - \mathrm{E}_\lambda[\langle \mathbf{D} \rangle]^2. \tag{7}$$

The impact of averaging over microenvironment tensors is determined by the size of the averaging volume, i.e., the voxel size, where larger voxels tend to reduce the macroscopic anisotropy in tissues that are not perfectly coherent (De Santis et al., 2013; Szczepankiewicz et al., 2015; Vos et al., 2011). Assuming that a voxel contains only one type of tissue, i.e., that the microenvironments differ only in orientation, the μFA is independent of the voxel size and may be interpreted as the FA that would be observed if the tissue exhibited complete orientation coherence, i.e., that all anisotropic structures were parallel (Jespersen et al., 2013; Lasič et al., 2014; Szczepankiewicz et al., 2015).

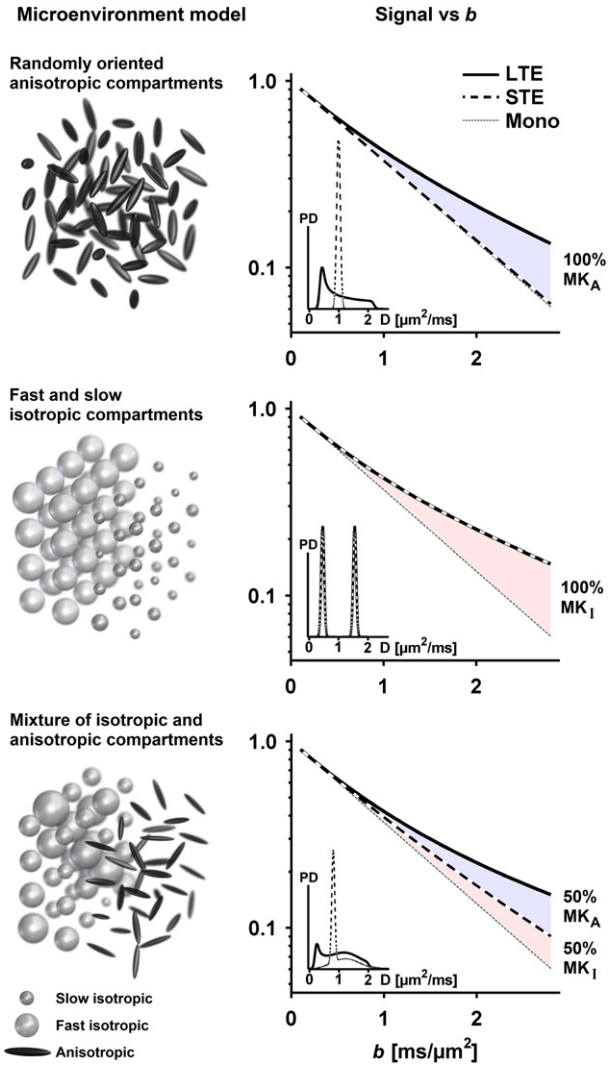

Fig. 1. Simulated tissue models that contain variable levels of microscopic anisotropy and isotropic heterogeneity. The first model contains randomly oriented anisotropic microenvironments, designed to mimic eccentric and disordered cells. The second model contains microenvironments with slow and fast isotropic diffusion, designed to mimic a mixture of high and low cell density. The third model is a mixture of the previous two. The right column shows the signal vs *b* curves in each case, where linear and spherical tensor encoding (LTE and STE) are shown as solid and broken lines, respectively. The dotted line shows mono-exponential signal decay for visual reference. The light blue and red fields accentuate the effect of microscopic anisotropy and isotropic heterogeneity, respectively. The inset plots show the distributions of apparent diffusion coefficients when using LTE (solid line) and STE (broken line), where the y-axis is the unitless probability density (PD). All three models have MD = 1.0 μm²/ms, and $\mathrm{MK_T} = 0.6$, and would thus be indistinguishable with LTE, i.e., conventional diffusion encoding. By adding isotropic encoding the three environments can be distinguished and the measured diffusional variance can be attributed to the appropriate microstructural feature.

Materials and methods

Patient population

Patients were recruited and scanned between October 2013 and October 2014. The study was approved by the Regional Ethical Review

Board at Lund University, and written consent was obtained from all patients prior to participation. Patients with suspected meningioma or glioma based on radiological findings, who were scheduled for surgical treatment, were considered for inclusion. The sample size was determined by the number of participating patients who were histologically confirmed to have a meningioma or glioma. In total, 14 patients were included. One patient had both a meningioma and a glioma and was therefore included in both groups. The meningioma group comprised 7 patients (6 women, 1 man; mean age ± s.d., 66 ± 11 years), and the glioma group 8 patients (5 women, 3 men; 54 ± 14 years). One patient from each group was analyzed and presented in a preliminary study (Szczepankiewicz et al., 2015), and several were also included in an independent study on water exchange (Lampinen et al., 2016). The tumors were graded according to the World Health Organization guidelines (Louis et al., 2007), resulting in 6 grade I, and 1 grade II meningiomas; and 1 grade II, 3 grade III, and 4 grade IV gliomas. Of the meningiomas, four were fibroblastic, two were transitional, and one was atypical (Riemenschneider et al., 2006). Due to the small number of subjects, associations between parameters and tumor grade were not investigated.

MRI data acquisition and analysis

MRI data was acquired using a Philips Achieva 3T system, equipped with 80 mT/m gradients with a maximum slew rate of 100 mT/m/ms, and an eight-channel receiver head-coil. The dMRI sequence was identical to that reported by Szczepankiewicz et al. (2015). Briefly, we used linear and spherical tensor encoding at ten equidistant b-values between 100 and 2800 s/mm^2. The LTE was performed in 15 directions, distributed on the half-sphere using electrostatic repulsion (Jones et al., 1999). The STE was achieved by magic angle spinning of the q-vector (qMAS) (Eriksson et al., 2013), and was repeated 15 times per b-value without rotation since it is assumed to be independent of rotation. The sequence had an echo time of 160 ms where the diffusion encoding lasted 62.5 ms before and after the refocusing pulse, and were separated by approximately 9 ms. The b-value was adjusted by modulating the gradient amplitude. We note that significantly shorter encoding and echo times are possible by using optimized waveforms, rather than repeating the qMAS waveform before and after the refocusing pulse (Sjölund et al., 2015). All images were acquired using a repetition time of 2000 ms, 96 × 96 acquisition matrix, spatial resolution of 3 × 3 × 3 mm^3, partial Fourier factor of 0.8, and a SENSE factor of 2. The image volume contained five axial slices centered on the tumor. In the patient with both meningioma and glioma, the slices were placed slightly off the axial plane to include both tumors. Total scan time for LTE and STE was approximately 10 min. All data was corrected for motion and eddy-currents in ElastiX (Klein et al., 2010) using extrapolated reference images (Nilsson et al., 2015). Whole-brain morphological T1-weighted, and T2-weighted fluid-attenuated inversion recovery (FLAIR) sequences were acquired, as well as gadolinium-enhanced T1-weighted images as part of clinical routine.

Diffusional variance decomposition was used to estimate MD, V_T, V_A and V_I (Lasič et al., 2014). In this method the inverse Laplace transform of the gamma distribution function (Röding et al., 2012) is fitted to the powder average of the diffusion weighted signal (S), according to

$$S(b) = S_0\left(1 + b\frac{V}{\mathrm{MD}}\right)^{-\frac{\mathrm{MD}^2}{V}}, \tag{8}$$

where S_0 is the signal at $b = 0$ s/mm^2, and V is the observed variance. The powder average is used to remove the effects of orientation coherence, and is calculated by averaging the signal across all diffusion directions at each b-value (Edén, 2003; Lasič et al., 2014; Szczepankiewicz et al., 2016b). As described in the theory, the observed variance in Eq. 8 depends on the shape of the encoding tensor, according to

$$V = V_I + f \cdot V_A\,, \tag{9}$$

where f is the encoding shape factor; for linear and spherical tensor encoding, $f = 1$ and 0, respectively (Topgaard, 2016). Other encoding shapes can also be used, for example, DDE that renders axially symmetric prolate encoding tensors, i.e., planar tensor encoding (PTE), where $f = 1/4$ (Topgaard, 2016). The fitting was weighted to suppress the effect of signal attenuated below 10% of its initial value in order to alleviate effects of non-Gaussian phase distribution (Topgaard and Söderman, 2003) and the noise floor (Gudbjartsson and Patz, 1995). The fitting software is available online at https://github.com/markus-nilsson/md-dmri. The normalized variance was calculated according to Eq. 4, and we note that MK_T and the mean kurtosis, derived from conventional DKI, are representations of the same phenomenon although their numerical values are expected to differ due to differences in signal parameterization (Lätt et al., 2007). To elucidate the connection between diffusional anisotropy on the voxel- and microscopic scale, we also interpret the diffusional variance in terms of the fractional anisotropy, i.e., FA and μFA, respectively. The FA was calculated from Eq. 5, where the voxel scale tensor $\langle \mathbf{D} \rangle$ was estimated through conventional DTI analysis (Basser et al., 1994) based on LTE at $b \leq 1000$ s/mm^2. The μFA was calculated from Eq. 6 by substituting the eigenvalue mean and variance for the expressions in Eqs. 1, 3 and 7, according to

$$\mu\mathrm{FA} = \sqrt{\frac{3}{2}}\left(1 + \frac{\mathrm{MD}^2 + V_I}{\frac{5}{2}V_A}\right)^{-\frac{1}{2}}. \tag{10}$$

Note that the μFA in Eq. 10 is defined according to Westin et al. (2016), and differs slightly from the definition used by Lasič et al. (2014) and Szczepankiewicz et al. (2015).

The solid part of each tumor was manually defined in a region of interest (ROI) by an experienced neuroradiologist using anatomical, contrast-enhanced, and diffusion-weighted images for guidance. The operator was instructed to avoid including edema, confluent necroses, corticospinal fluid, and brain tissue that appeared healthy. The parameter mean across all included voxels was calculated for each tumor.

Histological preparation and quantitative microscopy

All tumors were resected 1 day after the MRI procedure and the preparation of tissue was performed according to clinical routine. Each tumor was fixed in 4% buffered formaldehyde solution and embedded in paraffin. The tissue specimens were sectioned at 4 μm through the bulk of the tumor, and stained with hematoxylin and eosin (H&E). Automated microscopy was performed on an Aperio ScanScope AT Turbo. All samples were scanned at ×20 magnification at a spatial resolution of 1.0 μm/pixel and a complete image was stitched together by vendor software. Tumor specimens ranged in size between 8 and 28 mm across, resulting in at most 780 megapixels per image.

The presence of anisotropic tissue structures was quantified with structure tensor analysis of histological images (Bigun, 1987; Budde and Annese, 2013; Budde and Frank, 2012; Khan et al., 2015). Briefly, the two-dimensional structure tensors ($\mathbf{S}$) were calculated for each pixel from the spatial derivative of the image in a given neighborhood defined by the size of a discrete Gaussian derivative filter (Bigun, 1987). We assume that the structure tensors reflect the local diffusion anisotropy and orientation, in accordance with similar studies of neural tissue (Budde and Frank, 2012; Khan et al., 2015). Thus, analogues to MK_A, μFA and FA can be calculated from the structure tensors. The standard deviation of the Gaussian derivative filter was set to 1 μm. To visualize coherent structures spanning the distance of diffusing water

during one imaging experiment, the structure tensor field was convolved with another Gaussian kernel with a standard deviation of 20 μm. This is adjusted to approximately match the root mean square displacement of water molecules in the tissue assuming a diffusivity of 2 μm^2/ms and diffusion time of 100 ms. The normalized variance of structure tensor eigenvalues (H_A) was calculated from Eq. 3 and Eq. 4, where we hypothesize that H_A across an appropriate length scale is proportional to MK_A, according to

$$H_A = 3 \cdot \frac{\langle V_\lambda[\mathbf{S}] \rangle}{\langle E_\lambda[\mathbf{S}] \rangle^2} \propto MK_A. \quad (11)$$

The structure tensor analogues to FA and μFA (FA_{ST} and μFA_{ST}) were calculated by inserting **S** into Eq. 5 and Eq. 6, respectively, where the factor 3/2 was replaced by 2 to scale the parameters to the interval 0 to 1. We note that the relation between parameters derived from 2D and 3D tensors are not straight forward (see Kingsley (2006) for a comprehensive review), however, we may assume that **D** and **S** are both sensitive to tissue anisotropy and should therefore be correlated (Budde and Frank, 2012). Note that in contrast to dMRI, we can access the structure tensor field at the resolution of a single microenvironment, and must therefore construct the macroscopic structure tensor **S** by averaging the tensor field across an appropriate area in order to allow comparison with **D** and its parameters. Unless stated otherwise, all structure tensor anisotropy parameters were calculated from an averaged structure tensor field with spatial resolution 3 × 3 mm^2, to mimic the resolution of the dMRI data.

The analogue to MK_I was calculated by assuming that the isotropic diffusivity of a microenvironment is related to the local cell density. This assumption is based on previous observations where cell density has been negatively correlated to the apparent diffusivity (Chenevert et al., 2000; Kinoshita et al., 2008; Padhani et al., 2009; Sugahara et al., 1999). Thus, we hypothesize that the distribution of isotropic diffusivities within a voxel is determined by the cell density distribution (ρ_c), and that the normalized variance of cell densities from microscopy (H_I) across an appropriate length scale, is proportional to MK_I, according to

$$H_I = 3 \cdot \frac{V[\rho_c]}{\langle \rho_c \rangle^2} \propto MK_I. \quad (12)$$

The local density of cells was calculated as the number of cell nuclei per unit area. The cell nuclei were automatically segmented and counted in tissue sub-sections of 300 × 300 μm^2, as described by Al-Kofahi et al. (2010). The detection of red blood cells was suppressed by using only the red channel of the original H&E stained image, and the detection of psammoma grains was suppressed by removing features with areas above 900 μm^2. Clustered nuclei were separated using the watershed algorithm (Malpica et al., 1997). Maps of H_I were calculated from the distribution of cell densities across 10 × 10 subsections, which yielded a spatial resolution of 3 × 3 mm^2.

The mean parameter values in each tumor were calculated across all tumor tissue in each section. To avoid the inclusion of empty space, and artefacts due to edge effects, hemorrhage, knife scoring, and folding, the parameter maps were masked based on manually adjusted image intensity thresholding.

Statistical analysis

The associations between parameters derived from dMRI and their corresponding variants derived from microscopy, i.e., MK_A vs H_A, MK_I vs H_I, FA vs FA_{ST}, and μFA vs μFA_{ST}, were estimated using linear correlation. Pearson's correlation coefficient (r) was used to describe the strength of the correlation and the threshold for significance was set to $\alpha = 0.05$. For simplicity, the measurement uncertainty in the independent variables (from microscopy) was assumed to be negligible. We note that MK_A and μFA are closely related and are expected to render similar correlations. Nevertheless, the μFA is presented in addition to the MK_A to provide a straightforward microscopic analogue to the FA. A multiple linear regression analysis was used to investigate which histological features were significant predictors for the outcome of the variance detected through dMRI. The analysis was performed separately for MK_T, MK_A and MK_I where the regression model was defined according to $MK_x = m + \beta_A H_A + \beta_I H_I$. The threshold for considering H_A and/or H_I to be significant predictors was set to $\alpha = 0.05$. The intercept, m, was not interpreted.

The diffusional variance, and its components, were explored between and within tumor groups. The dominant source of variance was established by comparing MK_A and MK_I within each group. The variance parameter that best distinguished between tumor types was established by estimating the 95% confidence interval of the absolute effect ($CI_{95\%}$), and Cohen's d (d, normalized by the pooled standard deviation). Thus, a total of five t-tests were performed (two tails, independent samples, not assuming equal variance, significance threshold $\alpha = 0.05$). The fact that one patient appeared in both tumor groups was assumed to have a negligible effect on the statistical analysis. Thus, samples taken from this patient were considered to be independent throughout the analysis. All statistical analysis was performed in MATLAB (R2013b, The Mathworks, Natick, MA).

Results

We performed dMRI in vivo in 7 meningiomas and 8 gliomas, and DIVIDE was used to probe the microscopic anisotropy and isotropic heterogeneity of the tumor tissue. Fig. 2 shows DIVIDE parameter maps (MK_T, MK_A and MK_I) in a meningioma and a glioma. Both tumors exhibited elevated MK_T, which indicated that both tumors are heterogeneous, although the specific source of heterogeneity cannot be established from MK_T. By contrast, the source of tumor heterogeneity was distinguishable based on the MK_A and MK_I, where the diffusional variance in the meningioma was dominated by the anisotropic component, and primarily due to isotropic heterogeneity in the glioma. The difference between tumors was also clearly discernible from the signal vs b curves in the two tumor ROIs. In the meningioma, the signal from linear and spherical encoding diverges, which indicates microscopic anisotropy (compare to first model in Fig. 1); whereas both types of encoding exhibit similar divergence from mono-exponential decay in the glioma, which indicates isotropic heterogeneity (compare to second model in Fig. 1). Overall, the DIVIDE parameters showed that the meningiomas comprised a microstructure that yielded prominent microscopic diffusion anisotropy, whereas the gliomas did not. The estimated mean [min, max] signal-to-noise ratio of the STE signal across all tumor ROIs was 39 [19, 75] at $b = 0$ s/mm^2, and 5.5 [3.0, 10] at the highest b-value where at least 10% signal remained, indicating that the data quality was sufficient for the analysis (Gudbjartsson and Patz, 1995). Furthermore, using 15 diffusion encoding directions was sufficient to render a rotationally invariant powder average since all tumors exhibited a relatively low voxel scale anisotropy (all tumors had a mean FA below 0.5) (Szczepankiewicz et al., 2016b).

All tumors were resected, and quantitative microscopy was used to measure the cell eccentricity and cell density in sections through the bulk of the tumor tissue. Fig. 3 shows quantitative microscopy parameter maps derived from structure tensor analysis and cell nuclei segmentation at the nominal resolution (1 × 1 μm^2) in a meningioma and a glioma. Fig. 3 also presents the structure tensors, orientation field, and cell nuclei outlines in magnified subsections of each tumor. Overall, the meningiomas comprised prominently eccentric cells and cell structures, while gliomas contained few, or no, such structures. The meningiomas exhibited variable anisotropy within and between tumors, where patches of coherent fascicles were mixed with highly disordered tissue (Fig. 3). By contrast, the gliomas exhibited low and relatively homogeneous structural anisotropy throughout the section, as well as regions

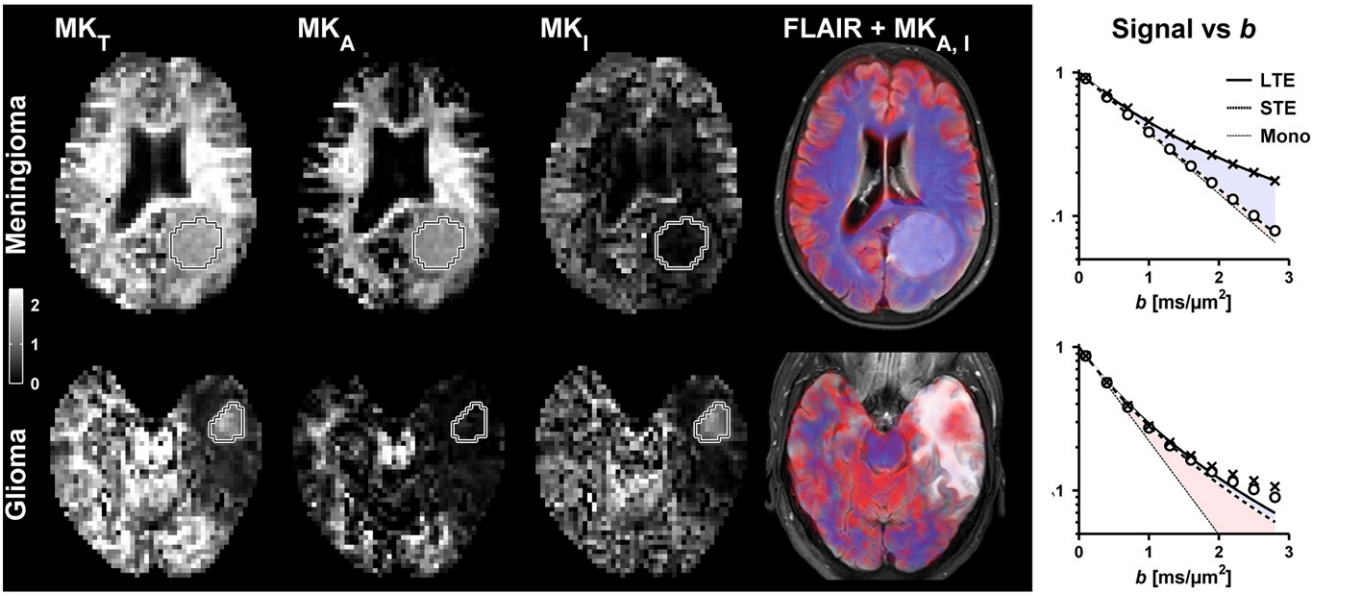

Fig. 2. Examples of DIVIDE parameter maps in a meningioma and a glioma. MK_T is elevated in both tumors but cannot distinguish between the isotropic and anisotropic components. By contrast, MK_A and MK_I are markedly different in the two tumors. These parameter maps were superimposed on a high resolution morphological image (FLAIR + $MK_{A,I}$), where MK_A and MK_I are coded in blue and red, respectively. The meningioma exhibited high MK_A and low MK_I (blue), whereas the opposite is true in the glioma (red). In the white matter the diffusional variance is mostly due to microscopic anisotropy, whereas the isotropic heterogeneity dominates in gray matter and voxels that contain both tissue and cerebrospinal fluid. The powder averaged signal vs *b* curves are shown in the rightmost column. The white-black outline shows the ROIs used for analysis. Note that the signal characteristics in the meningioma and glioma resemble the first and second models in Fig. 1, respectively.

of heterogeneous cell density, especially in necrotic regions (Fig. 3). The spatial heterogeneity of cell eccentricity and density within each tumor in Fig. 3 visualizes the need to analyze large tissue sections because small sub-sections may inadvertently sample regions of tissue that are not representative, leading to a large sampling error.

The parameters derived from dMRI were validated by correlating them to corresponding parameters from quantitative microscopy. All tests showed strong positive correlations, which indicates that the two components of diffusional variance indeed reflect specific features of the underlying microstructure. Fig. 4 shows scatterplots of the variance parameters where the strength of the correlation was $r = 0.95$ for MK_A ($p < 10^{-7}$) and $r = 0.83$ for MK_I ($p < 10^{-3}$). Similarly, Fig. 5 shows that both voxel-scale and microscopic parameters were correlated, where $r = 0.80$ for FA ($p < 10^{-3}$) and $r = 0.93$ for μFA ($p < 10^{-6}$). Furthermore, the regression analysis showed that both H_A and H_I were significant predictors for MK_T, where the estimated coefficients ± s.d. were $\beta_A =$

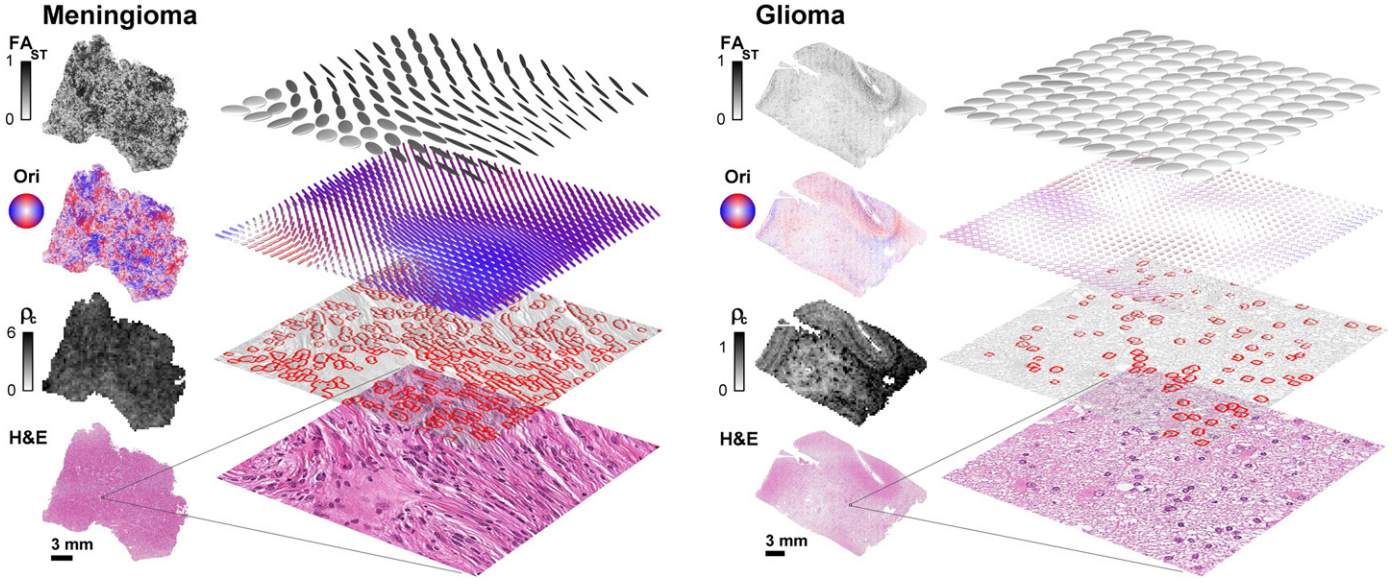

Fig. 3. Quantitative microscopy in a meningioma and a glioma. The full-section images show the structure tensor fractional anisotropy (FA_{ST}), orientation (Ori), cell density (ρ_c, $10^3/mm^2$), and the hematoxylin and eosin stain (H&E) in a meningioma and a glioma. Along with each map we visualize the tensor field, orientation field, cell outlines and H&E stain in a magnified sub-section ($300 \times 300\ \mu m^2$) of the tissue. The meningioma is grade I, fibroblastic subtype, with abundant anisotropic structures organized in large fascicles that render anisotropic diffusion. It has a high cell density and low density variance, i.e., the cell density map is uniform. The glioma is grade IV glioblastoma with few structures that are anisotropic, however, weakly coherent regions are observed in the normal-appearing cortex. The tumor tissue has a relatively low cell density and comprises large necrotic regions which exhibit highly variable cell density, i.e., the cell density map is non-uniform. The glioma is surrounded by cortical gray matter wherein the cortical layers can be partially distinguished in the cell-density map. Note that the anisotropy and orientation maps are calculated at $1 \times 1\ \mu m^2$ resolution, whereas the cell density is calculated at $300 \times 300\ \mu m^2$. Furthermore, the orientation map and orientation field are color coded to indicate local direction and anisotropy (color shows direction, saturation shows local FA_{ST}).

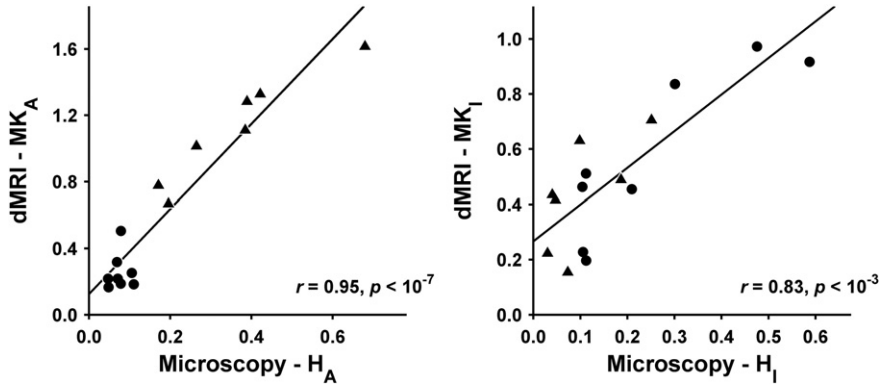

Fig. 4. Correlation between variance parameters derived from dMRI and microscopy in meningiomas (triangles) and gliomas (circles). The anisotropic and isotropic components of diffusional variance (MK_A and MK_I) exhibit strong positive correlations to structural anisotropy and cell density variance (H_A and H_I), respectively. Note that H_A and H_I are derived from structure tensor analysis and cell nuclei segmentation, respectively.

2.7 ± 0.4 ($p < 10^{-4}$) and $\beta_I = 1.4 \pm 0.4$ ($p < 10^{-2}$), respectively. This supports the notion that MK_T is not specific to either type of heterogeneity because it composes them into a single value. A more specific link between parameters was achieved by DIVIDE, where each variance component was significantly predicted by the corresponding microstructural features; the only significant predictor for MK_A was H_A, where $\beta_A = 2.5 \pm 0.3$ ($p < 10^{-6}$) and $\beta_I = 0.0 \pm 0.3$ ($p = 0.9$); the only significant predictor for MK_I was H_I, where $\beta_I = 1.4 \pm 0.3$ ($p < 10^{-3}$) and $\beta_A = 0.1 \pm 0.3$ ($p = 0.6$).

The comparison of diffusional variance within and between tumor groups is shown in Fig. 6 and Table 1. The microscopic anisotropy dominated in the meningiomas ($MK_A = 1.11 \pm 0.33$ vs $MK_I = 0.44 \pm 0.20$, $p < 10^{-3}$), whereas isotropic heterogeneity dominated in the gliomas ($MK_I = 0.57 \pm 0.30$ vs $MK_A = 0.26 \pm 0.11$, $p = 0.02$). Between tumor groups, MK_T and MK_A were found to be significantly higher in meningiomas (both $p < 10^{-3}$), while MK_I was not significantly different ($p = 0.3$). The largest effect size was found for MK_A where $d = 3.6$, compared to $d = 2.2$ for MK_T (see Table 1 for details). These findings suggest that the most prominent difference between the meningioma and glioma groups is driven by the presence or absence of microscopic anisotropy. To facilitate future comparisons we also report remaining parameters derived from dMRI and microscopy in Table 2.

Discussion

In this study, we used DIVIDE to decompose the anisotropic and isotropic components of the diffusional variance in meningioma and glioma tumors, and we pinpointed the source of these components through an independent analysis of the underlying microstructure. The MK_A parameter was shown to capture the structural anisotropy on the microscopic scale, where the diffusion anisotropy in the meningiomas was likely caused by an abundance of eccentric cells and cell structures. In agreement with preliminary results reported by Szczepankiewicz et al. (2015), such structures were absent in the gliomas. The MK_I parameter was shown to capture heterogeneous cell density which was caused by local patches of high and low cell density due to aggressive cell growth or necrosis. The strong correlations between parameters derived from dMRI and microscopy provide compelling evidence that MK_A, μFA and MK_I can be interpreted in terms of specific and intuitive features of tissue microstructure (Fig. 4). Furthermore, the regression analysis confirmed that MK_T conflates the effects of cell eccentricity and variable density (Mitra, 1995), and therefore lacks specificity, whereas MK_A and MK_I were specific to either of the two. Thus, the lack of specificity exhibited by MK_T can be recovered by decomposing MK_T into MK_A and MK_I. The FA and μFA also exhibited strong correlations

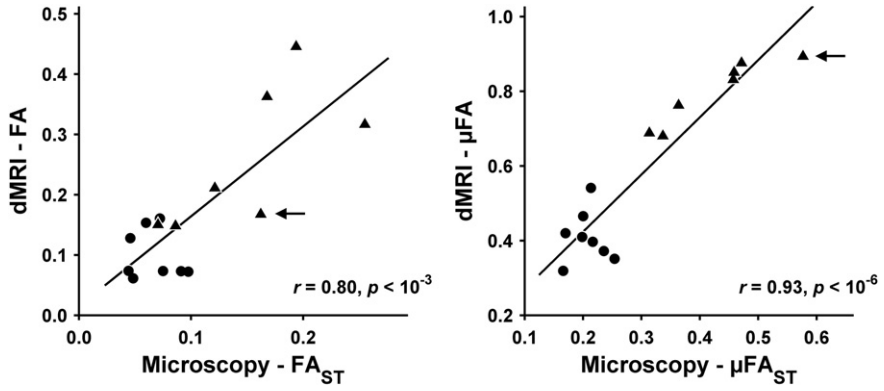

Fig. 5. Correlation between anisotropy parameters derived from dMRI and microscopy in meningiomas (triangles) and gliomas (circles). The diffusion anisotropy exhibits strong positive correlations with structure tensor anisotropy on the voxel (FA) and microscopic scale (μFA). Gliomas exhibit low FA and μFA, in agreement with the structure tensor analysis. By contrast, meningiomas exhibit a wide range of FA values, and relatively high μFA values. This suggests that the FA observed in meningiomas is strongly dependent on the orientation coherence of the tissue. The FA in meningiomas and gliomas may therefore overlap, impeding the ability of FA to differentiate the two tumor types despite their obvious difference in microscopic anisotropy. By contrast, the μFA clearly distinguishes the two tumor types. Moreover, the μFA stratified the fibroblastic meningiomas from the other subtypes, i.e., the fibroblastic tumors had the four highest μFA values, whereas the same stratification was not observed for FA. It may therefore be possible to use μFA for pre-surgical toughness estimation in meningiomas (Kashimura et al., 2007; Tropine et al., 2007). We emphasize that the tissue with the highest μFA is not necessarily mapped to the highest FA due to variable orientation coherence (black arrows point to the same tumor sample).

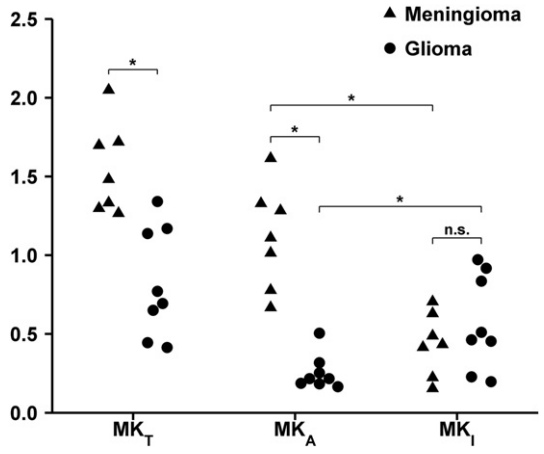

Fig. 6. Diffusional variance parameter distributions in the meningioma and glioma groups. Each data point shows the mean parameter value across all voxels in the tumor ROI. In the comparison between tumor groups, MK_T and MK_A were significantly different, whereas MK_I was not (* indicates statistical significance, n.s. indicates no significance; see Table 1 for details). Most notably, MK_A exhibits a distinct separation between the meningioma and glioma groups, indicating that the presence of anisotropic microstructures can be used to effectively differentiate the tumors. The comparison of MK_A and MK_I within tumor groups revealed that MK_A is dominant in the meningiomas, and MK_I is dominant in the gliomas.

with their structure tensor analogues (Fig. 5). This result is in accordance with similar studies performed in animals where voxel-scale diffusion anisotropy parameters, at high resolution, correlate with structure tensor anisotropy (Budde and Frank, 2012; Khan et al., 2015). However, here we show that the correlation also extends to measures of microscopic anisotropy and isotropic heterogeneity, which to our knowledge, have not been investigated previously.

The difference between the FA and μFA in the meningiomas is likely explained by the interaction between orientation coherence and voxel size (Oouchi et al., 2007). Fig. 7 utilizes the high-resolution microscopy images to demonstrate how larger voxels cause the FA in complex tissue to decrease due to a decreasing orientation coherence. It also highlights that this limitation can be mitigated by methods, such as DIVIDE, that recover the microscopic anisotropy (Jespersen et al., 2013; Lasič et al., 2014; Lawrenz and Finsterbusch, 2015; Westin et al., 2016). Thus, when interpreting voxel-scale anisotropy parameters such as the FA, the orientation coherence of the tissue is a potential confounder (De Santis et al., 2013).

Probing MK_A and MK_I separately revealed that the variance in meningioma tumors arises mainly due to the presence of anisotropic cell structures, whereas it was mainly due to isotropic heterogeneity in the gliomas (Fig. 6 and Table 1). Furthermore, MK_A exhibited the largest

Table 1
DIVIDE parameters in meningiomas and gliomas. Values are presented as group mean ± one standard deviation. For t-tests performed within and between groups we present the corresponding Cohen's d (d), 95% confidence interval ($CI_{99\%}$), and p-value (p). For meningiomas the dominant component was MK_A, whereas in gliomas the MK_I was dominant. Between tumor groups MK_T and MK_A differed significantly, where the MK_A exhibited the largest effect size. No significant difference between tumor types was found for MK_I.

		Meningioma	Glioma	Meningioma vs Glioma		
		($n = 7$)	($n = 8$)	$CI_{95\%}$	d	p
	MK_T	1.55 ± 0.29	0.83 ± 0.35	[0.37 1.08]	2.2	$<10^{-3}$
	MK_A	1.11 ± 0.33	0.26 ± 0.11	[0.55 1.16]	3.6	$<10^{-3}$
	MK_I	0.44 ± 0.20	0.57 ± 0.30	[−0.42 0.15]	−0.5	0.3
MK_A vs MK_I	$CI_{95\%}$	[0.35 1.00]	[−0.57 −0.06]			
	d	2.5	−1.4			
	p	$<10^{-3}$	0.02			

MK_T, total mean kurtosis; MK_A, anisotropic kurtosis; MK_I, isotropic kurtosis.

Table 2
Parameters derived from DTI, DIVIDE and quantitative microscopy in meningiomas and gliomas. Values are presented as group mean ± one standard deviation. The MD is in $\mu m^2/ms$, the ρ_c is in $10^3/mm^2$, remaining parameters are unitless.

	Meningioma	Glioma
	($n = 7$)	($n = 8$)
MD	1.08 ± 0.13	1.60 ± 0.22
FA	0.26 ± 0.12	0.10 ± 0.04
μFA	0.80 ± 0.09	0.41 ± 0.07
$<\rho_c>$	3.4 ± 1.8	2.2 ± 2.4
H_A	0.36 ± 0.17	0.08 ± 0.02
H_I	0.14 ± 0.09	0.11 ± 0.11
FA_{ST}	0.15 ± 0.06	0.07 ± 0.02
μFA_{ST}	0.43 ± 0.09	0.21 ± 0.03

MD, mean diffusivity; FA, fractional anisotropy; μFA, microscopic FA; $<\rho_c>$, cell density; H_A, normalized variance of structure tensor eigenvalues; H_I, normalized variance of cell density; subscript 'ST' denotes parameters derived from structure tensor analysis.

effect size between meningioma and glioma groups. This indicates that the primary difference between meningiomas and gliomas is the presence of structures that yield anisotropic diffusion at the microscopic scale, while the difference in isotropic heterogeneity is secondary (Table 1). In a statistical sense, MK_A should therefore be a superior biomarker compared to MK_T whenever the difference between tissues is predominately due to microscopic anisotropy. In such circumstances the MK_I may be considered a nuisance parameter; removing it increases the separation between groups resulting in a higher statistical power (Szczepankiewicz et al., 2013). Although removing one component of variance may improve the statistical power of studies aimed to find a specific effect, we stress that this is contextual. For example, a similar analysis applied to the white matter in schizophrenia patients considered the isotropic variance as the relevant component (Westin et al., 2016).

We expect that the improved specificity gained from decomposing the two sources of diffusional variance may be used to infer additional information about the underlying tissue microstructure, and may facilitate an improved interpretation of parameters that reflect diffusional

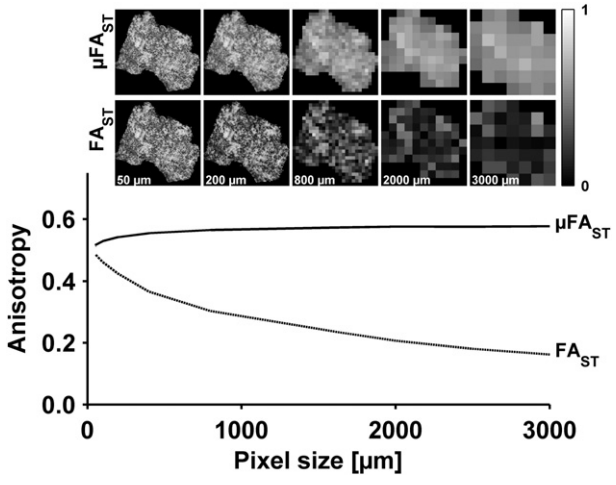

Fig. 7. Effect of spatial resolution and orientation coherence on anisotropy. The image array shows FA_{ST} and μFA_{ST} maps in a fibroblastic meningioma derived from the structure tensor field at spatial resolutions between 50 × 50 and 3000 × 3000 μm^2. The plotted lines show the average parameter values across the tumor section for the same interval of spatial resolutions. This showcases the interaction between the spatial resolution and the orientation coherence, where conventional anisotropy parameters, such as the FA from DTI, are reduced as the resolution decreases, in accordance with similar effects shown by Budde and Annese (2013). By contrast, the microscopic anisotropy, i.e., the μFA, remains stable and is independent of the spatial resolution. This demonstrates the inherent limitation of FA, and the advantage of μFA, when estimating anisotropy in complex tissue.

variance and kurtosis, as well as diffusion anisotropy. The method presented here is applicable to a wide variety of inquiries as it requires few assumptions about the investigated tissue and is implemented as a straight-forward modification to the conventional diffusion encoding sequence (Lasič et al., 2014; Szczepankiewicz et al., 2015). This is especially true if diffusion anisotropy parameters are intended to differentiate tumor subtypes (Jolapara et al., 2010; Sanverdi et al., 2012; Wang et al., 2012), preoperative estimation of tumor consistency (Kashimura et al., 2007; Tropine et al., 2007), delineation for biopsies (Kinoshita et al., 2008), and tumor proliferation (Beppu et al., 2005). Such cases warrant the use of MK_A or μFA, since conventional measures of anisotropy ignore the interaction between orientation coherence and voxel size, and may therefore be strongly biased (Fig. 7). This also extends to tissues outside of the central nervous system, such as the prostate where the stromal tissue is anisotropic and highly disordered on the sub-voxel scale (Bourne et al., 2012). Moreover, the ability to isolate the effects of isotropic heterogeneity may improve the characterization of tissue. For example, tumor infiltration in white matter may be better detected and delineated by removing the dominant effects of white matter anisotropy and instead characterizing the subtle changes in the isotropic heterogeneity (Sternberg et al., 2014).

We stress that the use of multiple encoding tensor shapes is required to probe the microscopic anisotropy and isotropic heterogeneity separately. As illustrated in Fig. 1, conventional encoding (LTE, solid lines) is theoretically incapable of distinguishing the three environments since all signal curves are virtually identical regardless of their anisotropic content (Mitra, 1995). Therefore, the microscopic anisotropy cannot be isolated by conventional encoding alone. This stands in contrast to Kaden et al. (2016) who claim that microscopic diffusion coefficients can be probed using only conventional SDE. Methods that attempt to estimate microscopic anisotropy and microscopic diffusion coefficients based only on SDE must either ignore the presence of isotropic diffusional variance, or assign values to it based on prior assumptions, e.g., assume that the system is composed of a mixture of specific microenvironments. However, since the isotropic variance exhibits considerable variation within individual subjects as well as between patients and controls (Szczepankiewicz et al., 2015), ignoring it will likely render an unpredictable bias that erroneously interprets isotropic heterogeneity as the presence of anisotropic structures, which impairs the interpretation of parameters such as the microscopic diffusion coefficients (Kaden et al., 2016).

We have identified three limiting aspects of the current study, pertaining to the generalization of the findings, the accuracy of the quantitative microscopy, and the clinical feasibility of the method. The generalization is limited because the present study comprises only two tumor types and a small number of tumors. Furthermore, the DIVIDE parameters may depend on features that are not included in the current models. For example, intra-voxel incoherent motion of blood may affect the diffusion weighted signal (Le Bihan et al., 1986). This may become relevant in well vascularized tumors, particularly since each waveform may contribute different levels of flow compensation (Ahlgren et al., 2016). The effects of water exchange across microenvironments could also affect the parameterization (Nilsson et al., 2013b). However, a preliminary study of the apparent exchange rate (Nilsson et al., 2013a) in meningiomas and gliomas reported residence times that were markedly longer than the diffusion times used in the current study (Lampinen et al., 2016), which suggests that the effects are negligible in these tumors. Restricted diffusion may yield an interaction between the diffusion time and the size distribution of restrictions (Gore et al., 2010). This may be especially relevant in diseased tissue where such features are unpredictable, and for non-conventional waveform shapes where the effective diffusion time is not well-defined (Nilsson et al., 2016). Although variable diffusion times normally have a limited influence in neural tissues (Nilsson et al., 2013b), integrating a model of restricted diffusion and DIVIDE may improve parameter accuracy (Ianus et al., 2016).

Several limitations pertain specifically to the quantitative microscopy. In the current implementation structural information is investigated in a two dimensional plane, whereas the diffusion takes place in three dimensions. This likely introduces a negative bias in structure anisotropy since through-plane anisotropy cannot be captured (Khan et al., 2015). Furthermore, 2D structure tensors cannot distinguish between structures that render oblate and prolate diffusion tensors which may impede the correlation between diffusion and structure tensors (Kingsley, 2006). More elaborate techniques based on confocal microscopy are able to reconstruct microscopic images in thin three dimensional slabs (Khan et al., 2015), however, these techniques were outside the scope of the present work. Although these limitations may impact the parameter accuracy, they may be partially mitigated by designing the microscopy-based metrics to be mathematically proportional to their dMRI analogues, and quantifying their association based on the strength of the correlation rather than the correspondence of absolute values.

The dMRI acquisition protocol reported in the present study was designed to oversample the directions and b-values for validation purposes (Szczepankiewicz et al., 2015) and therefore featured a relatively low spatial resolution and a long acquisition time at a limited slice coverage. A clinically feasible protocols can be achieved by reducing the number of b-values and by tailoring their distribution to the tissue of interest (Alexander, 2008; Knutsson and Westin, 2013; Szczepankiewicz et al., 2016b). For example, whole brain acquisition is possible at a resolution of $2 \times 2 \times 3$ mm^3 in less than 8 min by using only two non-zero b-values and optimized asymmetric waveforms (Sjölund et al., 2015), which can reduce the TE from 160 ms (presented herein) to below 100 ms (Szczepankiewicz et al., 2016a). Simultaneous multi-slice acquisitions could potentially reduce it below 4 min (Setsompop et al., 2012). The design of clinical protocols with respect to tissue characteristics and hardware capabilities will be addressed in future works.

Conclusions

We found an excellent agreement between DIVIDE parameters and tissue microstructure in meningiomas and gliomas. This constitutes compelling evidence that a link exists between diffusional variance and structural heterogeneity. The diffusional variance due to microscopic anisotropy and isotropic heterogeneity could be disentangled and linked specifically to cell eccentricity and cell density variance, where MK_A and μFA reflect cell eccentricity independent of orientation coherence, and MK_I reflects variable cell density. The separation of cell eccentricity from variable cell density relies on diffusion encoding tensors with multiple shapes and is therefore not accessible by methods based on conventional diffusion encoding, such as DKI. Thus, DIVIDE provides a more comprehensive and specific description of the tissue microstructure and heterogeneity, which can be used to improve the interpretation of diffusional variance and diffusional anisotropy.

Author contributions

All authors conceived and designed the study. MRI pulse sequence programming was done by FSz and MN. Patients were recruited by DvW and PS. Histological evaluation and quantitative microscopy was performed by FSz and EE. dMRI data was acquired and analyzed by FSz, DvW, JL and MN. Statistical evaluation was done by FSz and MN. All authors contributed to the writing of the manuscript.

Funding information

This research was supported by the Swedish Cancer Society (grant nos. CAN 2012/597 and CAN 2013/321), the Swedish Research Council (grant no. K2011-52X-21737-01-3), the Swedish Foundation for Strategic Research (grant no. AM13-0090), the National Institutes of Health

(grant nos. R01MH074794 and P41EB015902), the Swedish Brain Foundation (grant no. FO2014-0133), and CR Development AB (grant no. MN15).

Conflict of interest statement

MN declares research support from Colloidal Resource, and patent applications in Sweden (1250453-6 and 1250452-8), USA (61/642 594 and 61/642 589), and PCT (SE2013/050492 and SE2013/050493). Remaining authors declare no conflict of interest.

References

Ahlgren, A., Knutsson, L., Wirestam, R., Nilsson, M., Ståhlberg, F., Topgaard, D., Lasič, S., 2016. Quantification of microcirculatory parameters by joint analysis of flow-compensated and non-flow-compensated intravoxel incoherent motion (ivim) data. NMR Biomed. 29, 640–649.

Alexander, D.C., 2008. A general framework for experiment design in diffusion MRI and its application in measuring direct tissue-microstructure features. Magn. Reson. Med. 60, 439–448.

Alexander, A.L., Lee, J.E., Lazar, M., Field, A.S., 2007. Diffusion tensor imaging of the brain. Neurotherapeutics 4, 316–329.

Al-Kofahi, Y., Lassoued, W., Lee, W., Roysam, B., 2010. Improved automatic detection and segmentation of cell nuclei in histopathology images. IEEE Trans. Biomed. Eng. 57, 841–852.

Barazany, D., Basser, P.J., Assaf, Y., 2009. In vivo measurement of axon diameter distribution in the corpus callosum of rat brain. Brain 132, 1210–1220.

Basser, P.J., Pierpaoli, C., 1996. Microstructural and physiological features of tissues elucidated by quantitative-diffusion-tensor MRI. J. Magn. Reson. 209–2019.

Basser, P.J., Mattiello, J., Le Bihan, D., 1994. MR diffusion tensor spectroscopy and imaging. Biophys. J. 66, 259–267.

Beppu, T., Inoue, T., Shibata, Y., Yamada, N., Kurose, A., Ogasawara, K., Ogawa, A., Kabasawa, H., 2005. Fractional anisotropy value by diffusion tensor magnetic resonance imaging as a predictor of cell density and proliferation activity of glioblastomas. Surg. Neurol. 63, 56–61 (discussion 61).

Bigun, J., 1987. Optimal Orientation Detection of Linear Symmetry. Proc. of the IEEE First International Conference on Computer Vision, London. pp. 433–438.

Bourne, R.M., Kurniawan, N., Cowin, G., Sved, P., Watson, G., 2012. Microscopic diffusion anisotropy in formalin fixed prostate tissue: preliminary findings. Magn. Reson. Med. 68, 1943–1948.

Budde, M.D., Annese, J., 2013. Quantification of anisotropy and fiber orientation in human brain histological sections. Front. Integr. Neurosci. 7, 3.

Budde, M.D., Frank, J.A., 2012. Examining brain microstructure using structure tensor analysis of histological sections. NeuroImage 63, 1–10.

Callaghan, P.T., Komlosh, M.E., 2002. Locally anisotropic motion in a macroscopically isotropic system: displacement correlations measured using double pulsed gradient spin-echo nmr. Magn. Reson. Chem. 40, S15–S19.

Chenevert, T.L., Stegman, L.D., Taylor, J.M., Robertson, P.L., Greenberg, H.S., Rehemtulla, A., Ross, B.D., 2000. Diffusion magnetic resonance imaging: an early surrogate marker of therapeutic efficacy in brain tumors. J. Natl. Cancer Inst. 92, 2029–2036.

De Santis, S., Drakesmith, M., Bells, S., Assaf, Y., Jones, D.K., 2013. Why diffusion tensor MRI does well only some of the time: variance and covariance of white matter tissue microstructure attributes in the living human brain. NeuroImage 89C, 35–44.

Edén, M., 2003. Computer simulations in solid-state nmr. Iii. Powder averaging. Concepts in Magnetic Resonance Part A 18A, 24–55.

Eriksson, S., Lasič, S., Topgaard, D., 2013. Isotropic diffusion weighting in PGSE nmr by magic-angle spinning of the q-vector. J. Magn. Reson. 226, 13–18.

Eriksson, S., Lasič, S., Nilsson, M., Westin, C.F., Topgaard, D., 2015. Nmr diffusion-encoding with axial symmetry and variable anisotropy: distinguishing between prolate and oblate microscopic diffusion tensors with unknown orientation distribution. J. Chem. Phys. 142, 104201.

Gore, J.C., Xu, J., Colvin, D.C., Yankeelov, T.E., Parsons, E.C., Does, M.D., 2010. Characterization of tissue structure at varying length scales using temporal diffusion spectroscopy. NMR Biomed. 23, 745–756.

Gudbjartsson, H., Patz, S., 1995. The rician distribution of noisy MRI data. Magn. Reson. Imaging 910–914.

Ianus, A., Drobnjak, I., Alexander, D.C., 2016. Model-based estimation of microscopic anisotropy using diffusion MRI: a simulation study. NMR Biomed. 29, 672–685.

Jelescu, I.O., Zurek, M., Winters, K.V., Veraart, J., Rajaratnam, A., Kim, N.S., Babb, J.S., Shepherd, T.M., Novikov, D.S., Kim, S.G., Fieremans, E., 2016. In vivo quantification of demyelination and recovery using compartment-specific diffusion MRI metrics validated by electron microscopy. NeuroImage 132, 104–114.

Jensen, J.H., Helpern, J.A., Ramani, A., Lu, H., Kaczynski, K., 2005. Diffusional kurtosis imaging: the quantification of non-Gaussian water diffusion by means of magnetic resonance imaging. Magn. Reson. Med. 53, 1432–1440.

Jensen, J.H., Hui, E.S., Helpern, J.A., 2014. Double-pulsed diffusional kurtosis imaging. NMR Biomed. 27, 363–370.

Jespersen, S.N., Bjarkam, C.R., Nyengaard, J.R., Chakravarty, M.M., Hansen, B., Vosegaard, T., Østergaard, L., Yablonskiy, D., Nielsen, N.C., Vestergaard-Poulsen, P., 2010. Neurite density from magnetic resonance diffusion measurements at ultrahigh field: comparison with light microscopy and electron microscopy. NeuroImage 49, 205–216.

Jespersen, S.N., Lundell, H., Sønderby, C.K., Dyrby, T.B., 2013. Orientationally invariant metrics of apparent compartment eccentricity from double pulsed field gradient diffusion experiments. NMR Biomed. 26, 1647–1662.

Jolapara, M., Kesavadas, C., Radhakrishnan, V.V., Thomas, B., Gupta, A.K., Bodhey, N., Patro, S., Saini, J., George, U., Sarma, P.S., 2010. Role of diffusion tensor imaging in differentiating subtypes of meningiomas. J. Neuroradiol. 37, 277–283.

Jones, D.K., Horsfield, M.A., Simmons, A., 1999. Optimal strategies for measuring diffusion in anisotropic systems by magnetic resonance imaging. Magn. Reson. Med. 42, 515–525.

Kaden, E., Kruggel, F., Alexander, D.C., 2016. Quantitative mapping of the per-axon diffusion coefficients in brain white matter. Magn. Reson. Med. 75, 1752–1763.

Kamagata, K., Kerever, A., Yokosawa, S., Otake, Y., Ochi, H., Hori, M., Kamiya, K., Tsuruta, K., Tagawa, K., Okazawa, H., Aoki, S., Arikawa-Hirasawa, E., 2016. Quantitative histological validation of diffusion tensor MRI with two-photon microscopy of cleared mouse brain. Magn. Reson. Med. Sci.

Kashimura, H., Inoue, T., Ogasawara, K., Arai, H., Otawara, Y., Kanbara, Y., Ogawa, A., 2007. Prediction of meningioma consistency using fractional anisotropy value measured by magnetic resonance imaging. J. Neurosurg. 107, 784–787.

Khan, A.R., Cornea, A., Leigland, L.A., Kohama, S.G., Jespersen, S.N., Kroenke, C.D., 2015. 3d structure tensor analysis of light microscopy data for validating diffusion MRI. NeuroImage 111, 192–203.

Kingsley, P.B., 2006. Introduction to diffusion tensor imaging mathematics: part ii. Anisotropy, diffusion-weighting factors, and gradient encoding schemes. Concepts in Magnetic Resonance Part A 28A, 123–154.

Kinoshita, M., Hashimoto, N., Goto, T., Kagawa, N., Kishima, H., Izumoto, S., Tanaka, H., Fujita, N., Yoshimine, T., 2008. Fractional anisotropy and tumor cell density of the tumor core show positive correlation in diffusion tensor magnetic resonance imaging of malignant brain tumors. NeuroImage 43, 29–35.

Klein, S., Staring, M., Murphy, K., Viergever, M.A., Pluim, J.P., 2010. Elastix: a toolbox for intensity-based medical image registration. IEEE Trans. Med. Imaging 29, 196–205.

Knutsson, H., Westin, C.F., 2013. Tensor metrics and charged containers for 3d q-space sample distribution. Med. Image Comput. Comput. Assist. Interv. 16, 679–686.

Lampinen, B., Szczepankiewicz, F., van Westen, D., Englund, E., Sundgren, P., Lätt, J., Ståhlberg, F., Nilsson, M., 2016. Optimal experimental design for filter exchange imaging: apparent exchange rate measurements in the healthy brain and in intracranial tumors. Magn. Reson. Med.

Lasič, S., Szczepankiewicz, F., Eriksson, S., Nilsson, M., Topgaard, D., 2014. Microanisotropy imaging: quantification of microscopic diffusion anisotropy and orientational order parameter by diffusion MRI with magic-angle spinning of the q-vector. Front. Phys. 2, 11.

Lätt, J., Nilsson, M., Malmborg, C., Rosquist, H., Wirestam, R., Ståhlberg, F., Topgaard, D., Brockstedt, S., 2007. Accuracy of q-space related parameters in MRI: simulations and phantom measurements. IEEE Trans. Med. Imaging 26, 1437–1447.

Lawrenz, M., Finsterbusch, J., 2015. Mapping measures of microscopic diffusion anisotropy in human brain white matter in vivo with double-wave-vector diffusion-weighted imaging. Magn. Reson. Med. 73, 773–783.

Lawrenz, M., Koch, M.A., Finsterbusch, J., 2010. A tensor model and measures of microscopic anisotropy for double-wave-vector diffusion-weighting experiments with long mixing times. J. Magn. Reson. 202, 43–56.

Le Bihan, D., 2013. Apparent diffusion coefficient and beyond: what diffusion MR imaging can tell us about tissue structure. Radiology 268, 318–322.

Le Bihan, D., Breton, E., Lallemand, D., Grenier, P., Cabanis, E., Laval-Jeantet, M., 1986. MR imaging of intravoxel incoherent motions: application to diffusion and perfusion in neurologic disorders. Radiology 161, 401–407.

Louis, D.N., Ohgaki, H., Wiestler, O.D., Cavenee, W.K., Burger, P.C., Jouvet, A., Scheithauer, B.W., Kleihues, P., 2007. The 2007 who classification of tumours of the central nervous system. Acta Neuropathol. 114, 97–109.

Maier, S.E., Sun, Y., Mulkern, R.V., 2010. Diffusion imaging of brain tumors. NMR Biomed. 23, 849–864.

Malpica, N., de Solorzano, C.O., Vaquero, J.J., Santos, A., Vallcorba, I., Garcia-Sagredo, J.M., del Pozo, F., 1997. Applying watershed algorithms to the segmentation of clustered nuclei. Cytometry 28, 289–297.

Marusyk, A., Polyak, K., 2010. Tumor heterogeneity: causes and consequences. Biochimica et Biophysica Acta (BBA) - Reviews on Cancer 1805, 105–117.

Mitra, P., 1995. Multiple wave-vector extensions of the nmr pulsed-field-gradient spin-echo diffusion measurement. Phys. Rev. B 51, 15074–15078.

Moffat, B.A., Chenevert, T.L., Lawrence, T.S., Meyer, C.R., Johnson, T.D., Dong, Q., Tsien, C., Mukherji, S., Quint, D.J., Gebarski, S.S., Robertson, P.L., Junck, L.R., Rehemtulla, A., Ross, B.D., 2005. Functional diffusion map: a noninvasive MRI biomarker for early stratification of clinical brain tumor response. Proc. Natl. Acad. Sci. U. S. A. 102, 5524–5529.

Nilsson, M., Lätt, J., van Westen, D., Brockstedt, S., Lasič, S., Ståhlberg, F., Topgaard, D., 2013a. Noninvasive mapping of water diffusional exchange in the human brain using filter-exchange imaging. Magn. Reson. Med. 69, 1573–1581.

Nilsson, M., van Westen, D., Ståhlberg, F., Sundgren, P.C., Lätt, J., 2013b. The role of tissue microstructure and water exchange in biophysical modelling of diffusion in white matter. MAGMA 26, 345–370.

Nilsson, M., Szczepankiewicz, F., van Westen, D., Hansson, O., 2015. Extrapolation-based references improve motion and eddy-current correction of high b-value dwi data: application in Parkinson's disease dementia. PLoS One 10, e0141825.

Nilsson, M., Lasič, S., Topgaard, D., Westin, C.F., 2016. Estimating the axon diameter from intra-axonal water diffusion with arbitrary gradient waveforms: resolution limit in parallel and dispersed fibers. Proc. Int. Soc. Magn. Reson. Med. 24, 0663 (Singapore).

Oouchi, H., Yamada, K., Sakai, K., Kizu, O., Kubota, T., Ito, H., Nishimura, T., 2007. Diffusion anisotropy measurement of brain white matter is affected by voxel size: underestimation occurs in areas with crossing fibers. AJNR Am. J. Neuroradiol. 28, 1102–1106.

Ozarslan, E., Basser, P.J., 2008. Microscopic anisotropy revealed by nmr double pulsed field gradient experiments with arbitrary timing parameters. J. Chem. Phys. 128, 154511.
Padhani, A.R., Liu, G., Mu-Koh, D., Chenevert, T.L., Thoeny, H.C., Takahara, T., Dzik-Jurasz, A., Ross, B.D., Van Cauteren, M., Collins, D., Hammoud, D.A., Rustin, G.J.S., Taouli, B., Choyke, P.L., 2009. Diffusion-weighted magnetic resonance imaging as a cancer biomarker: consensus and recommendations. Neoplasia 11, 102–125.
Raab, P., Hattingen, E., Franz, K., Zanella, F.E., Lanfermann, H., 2010. Cerebral gliomas: diffusional kurtosis imaging analysis of microstructural differences. Radiology 254, 876–881.
Riemenschneider, M.J., Perry, A., Reifenberger, G., 2006. Histological classification and molecular genetics of meningiomas. The Lancet Neurology 5, 1045–1054.
Röding, M., Bernin, D., Jonasson, J., Sarkka, A., Topgaard, D., Rudemo, M., Nyden, M., 2012. The gamma distribution model for pulsed-field gradient nmr studies of molecular-weight distributions of polymers. J. Magn. Reson. 222, 105–111.
Ronen, I., Budde, M., Ercan, E., Annese, J., Techawiboonwong, A., Webb, A., 2014. Microstructural organization of axons in the human corpus callosum quantified by diffusion-weighted magnetic resonance spectroscopy of n-acetylaspartate and post-mortem histology. Brain Struct. Funct. 219, 1773–1785.
Ryu, Y.J., Choi, S.H., Park, S.J., Yun, T.J., Kim, J.H., Sohn, C.H., 2014. Glioma: application of whole-tumor texture analysis of diffusion-weighted imaging for the evaluation of tumor heterogeneity. PLoS One 9, e108335.
Sanverdi, S.E., Ozgen, B., Oguz, K.K., Mut, M., Dolgun, A., Soylemezoglu, F., Cila, A., 2012. Is diffusion-weighted imaging useful in grading and differentiating histopathological subtypes of meningiomas? Eur. J. Radiol. 81, 2389–2395.
Schilling, K., Janve, V., Gao, Y., Stepniewska, I., Landman, B.A., Anderson, A.W., 2016. Comparison of 3d orientation distribution functions measured with confocal microscopy and diffusion MRI. NeuroImage 129, 185–197.
Setsompop, K., Cohen-Adad, J., Gagoski, B.A., Raij, T., Yendiki, A., Keil, B., Wedeen, V.J., Wald, L.L., 2012. Improving diffusion MRI using simultaneous multi-slice echo planar imaging. NeuroImage 63, 569–580.
Shemesh, N., Ozarslan, E., Adiri, T., Basser, P.J., Cohen, Y., 2010. Noninvasive bipolar double-pulsed-field-gradient nmr reveals signatures for pore size and shape in polydisperse, randomly oriented, inhomogeneous porous media. J. Chem. Phys. 133, 044705.
Sjölund, J., Szczepankiewicz, F., Nilsson, M., Topgaard, D., Westin, C.F., Knutsson, H., 2015. Constrained optimization of gradient waveforms for generalized diffusion encoding. J. Magn. Reson. 261, 157–168.
Sternberg, E.J., Lipton, M.L., Burns, J., 2014. Utility of diffusion tensor imaging in evaluation of the peritumoral region in patients with primary and metastatic brain tumors. AJNR Am. J. Neuroradiol. 35, 439–444.
Sugahara, T., Korogi, Y., Kochi, M., Ikushima, I., Shigematu, Y., Hirai, T., Okuda, T., Liang, L.X., Ge, Y.L., Komohara, Y., Ushio, Y., Takahashi, M., 1999. Usefulness of diffusion-weighted MRI with echo-planar technique in the evaluation of cellularity in gliomas. Jmri-Journal of Magnetic Resonance Imaging 9, 53–60.
Szczepankiewicz, F., Lätt, J., Wirestam, R., Leemans, A., Sundgren, P., van Westen, D., Ståhlberg, F., Nilsson, M., 2013. Variability in diffusion kurtosis imaging: impact on study design, statistical power and interpretation. NeuroImage 76, 145–154.
Szczepankiewicz, F., Lasič, S., van Westen, D., Sundgren, P.C., Englund, E., Westin, C.F., Ståhlberg, F., Lätt, J., Topgaard, D., Nilsson, M., 2015. Quantification of microscopic diffusion anisotropy disentangles effects of orientation dispersion from microstructure: applications in healthy volunteers and in brain tumors. NeuroImage 104, 241–252.
Szczepankiewicz, F., Westin, C.F., Ståhlberg, F., Lätt, J., Nilsson, M., 2016a. Microscopic anisotropy imaging at 7 t using asymmetrical gradient waveform encoding. Proc. Int. Soc. Magn. Reson. Med. 24, 1081 (Singapore).
Szczepankiewicz, F., Westin, C.F., Ståhlberg, F., Lätt, J., Nilsson, M., 2016b. Minimum number of diffusion encoding directions required to yield a rotationally invariant powder average signal in single and double diffusion encoding. Proc. Int. Soc. Magn. Reson. Med. 24, 2065 (Singapore).
Tietze, A., Hansen, M.B., Ostergaard, L., Jespersen, S.N., Sangill, R., Lund, T.E., Geneser, M., Hjelm, M., Hansen, B., 2015. Mean diffusional kurtosis in patients with glioma: initial results with a fast imaging method in a clinical setting. AJNR Am. J. Neuroradiol. 36, 1472–1478.
Topgaard, D., 2016. Nmr methods for studying microscopic diffusion anisotropy. In: Valiullin, R. (Ed.), Diffusion NMR in Confined Systems: Fluid Transport in Porous Solids and Heterogeneous Materials. Royal Society of Chemistry, Cambridge, UK.
Topgaard, D., Söderman, O., 2003. Experimental determination of pore shape and size using q-space nmr microscopy in the long diffusion-time limit. Magn. Reson. Imaging 21, 69–76.
Tropine, A., Dellani, P.D., Glaser, M., Bohl, J., Ploner, T., Vucurevic, G., Perneczky, A., Stoeter, P., 2007. Differentiation of fibroblastic meningiomas from other benign subtypes using diffusion tensor imaging. J. Magn. Reson. Imaging 25, 703–708.
Van Cauter, S., Veraart, J., Sijbers, J., Peeters, R.R., Himmelreich, U., De Keyzer, F., Van Gool, S.W., Van Calenbergh, F., De Vleeschouwer, S., Van Hecke, W., Sunaert, S., 2012. Gliomas: diffusion kurtosis MR imaging in grading. Radiology 263, 492–501.
Vos, S.B., Jones, D.K., Viergever, M.A., Leemans, A., 2011. Partial volume effect as a hidden covariate in DTI analyses. NeuroImage 55, 1566–1576.
Wang, S., Kim, S., Zhang, Y., Wang, L., Lee, E.B., Syre, P., Poptani, H., Melhem, E.R., Lee, J.Y., 2012. Determination of grade and subtype of meningiomas by using histogram analysis of diffusion-tensor imaging metrics. Radiology 262, 584–592.
Westin, C.F., Knutsson, H., Pasternak, O., Szczepankiewicz, F., Özarslan, E., van Westen, D., Mattisson, C., Bogren, M., O'Donnell, L.J., Kubicki, M., Topgaard, D., Nilsson, M., 2016. Q-space trajectory imaging for multidimensional diffusion MRI of the human brain. NeuroImage 135, 345–362.
Wu, E.X., Cheung, M.M., 2010. MR diffusion kurtosis imaging for neural tissue characterization. NMR Biomed. 23, 836–848.